



Article

Contribution to Excitonic Linewidth from Free Carrier–Exciton Scattering in Layered Materials: The Example of hBN

Maurício F. C. Martins Quintela ^{1,2,*}  and Nuno M. R. Peres ^{1,2} 

¹ Department of Physics, Physics Center of Minho, Campus of Gualtar, Porto Universities (CF–UM–UP), 4710-057 Braga, Portugal

² International Iberian Nanotechnology Laboratory (INL), Av. Mestre José Veiga, 4715-330 Braga, Portugal

* Correspondence: mfcmquintela@gmail.com

Abstract: Scattering of excitons by free carriers is a phenomenon, which is especially important when considering moderately to heavily doped semiconductors in low-temperature experiments, where the interaction of excitons with acoustic and optical phonons is reduced. In this paper, we consider the scattering of excitons by free carriers in monolayer hexagonal boron nitride encapsulated by a dielectric medium. We describe the excitonic states by variational wave functions, modeling the electrostatic interaction via the Rytova–Keldysh potential. Making the distinction between elastic and inelastic scattering, the relevance of each transition between excitonic states is also considered. Finally, we discuss the contribution of free carrier scattering to the excitonic linewidth, analyzing both its temperature and carrier density dependence.

Keywords: exciton; linewidth; free carrier; monolayer; scattering; temperature; screening; hexagonal boron nitride; variational



Citation: Quintela, M.F.C.M.; Peres, N.M.R. Contribution to Excitonic Linewidth from Free Carrier–Exciton Scattering in Layered Materials: The Example of hBN. *Appl. Sci.* **2022**, *12*, 7872. <https://doi.org/10.3390/app12157872>

Academic Editor: Francesco Tornabene

Received: 18 July 2022

Accepted: 3 August 2022

Published: 5 August 2022

Publisher’s Note: MDPI stays neutral with regard to jurisdictional claims in published maps and institutional affiliations.



Copyright: © 2022 by the authors. Licensee MDPI, Basel, Switzerland. This article is an open access article distributed under the terms and conditions of the Creative Commons Attribution (CC BY) license (<https://creativecommons.org/licenses/by/4.0/>).

1. Introduction

Scattering between excitons and free carriers has been observed experimentally since the 1960s in highly excited bulk semiconductors [1–8]. In these bulk semiconductor systems, the scattering cross sections have been studied previously [9,10], with the distinction between elastic and inelastic scattering fundamental for the interpretation of the experimental data.

Recently, the quality of monolayer semiconductor samples has drastically increased [11–15], with advances in techniques such as molecular beam epitaxy [16], chemical vapor deposition [17], or solution methods [18]. The improved quality of these samples allows for a much more detailed study of excitons in mono- and few-layer materials, where well-defined resonance peaks are experimentally identifiable even at room temperature [19–22]. This then creates the necessity of calculating and measuring the excitonic linewidth.

Several mechanisms contribute to the excitonic linewidth, such as acoustic [23] and optical [24] phonon scattering [25], radiative recombination [26,27], as well as scattering in semiconductor alloys [28,29]. In addition to these mechanisms, others can play a part in determining the exciton linewidth. In this paper, we focus our attention on one of these mechanisms, namely scattering with free carriers. This scattering mechanism can play an important part in determining the excitonic linewidth, especially in systems with a high density of free carriers and excitons [30], high pump fluences [31], in tunneling experiments [32,33], or when an electric field is applied to the semiconductor [34,35]. Additionally, electron exciton scattering processes also play an important role when studying exciton–polaron systems [36].

This paper is structured as follows. In Section 2, we briefly review the approach outlined by Feng and Spector in Ref. [37] to the scattering between free carriers and excitons in semiconducting quantum wells. This derivation was performed in the central field [38] and Born approximations [39]. In Section 3, we turn our discussion to the

total scattering cross section. We discuss the distinction between elastic and inelastic scattering, briefly reviewing the variational exciton wave functions for various states. We then explicitly compute the total cross section for a few select transitions, discussing the thresholds present in inelastic scattering processes. Finally, in Section 4, we compute the contribution to excitonic linewidth from the scattering cross section with free carriers, analyzing its dependence on both the temperature of the system and the free carrier density in the monolayer.

2. Free Carrier–Exciton Scattering

In this section, we follow the expressions derived by Feng and Spector in Ref. [37] for free carrier–exciton scattering, based on assuming two-dimensional (2D) gases of free carriers (electrons or holes) and excitons interacting with one another. The obtained expressions are derived following the same approach as those discussed by Mott and Massey for the general theory for tridimensional (3D) two-body collisions [40]. The cross sections due to collisions between the carriers and excitons are then calculated using the central field [38] and Born approximations [39].

Differential Scattering Cross Section

Let us begin by considering a two-body system consisting of an exciton and a free carrier (electron or hole). The reduced mass of such a system is given by

$$M = \frac{m_c(m_e + m_h)}{m_c + m_e + m_h}, \quad (1)$$

where $m_{c/e/h}$ is the mass of the free carrier/electron/hole.

Following the derivations by Feng and Spector [37,41] detailed in Appendix A, the differential scattering cross section for our free carrier–exciton system is written as

$$I_{fi}(\theta) = \frac{M^2}{2\pi\hbar^4k_i} \left| \int d^2\mathbf{r} d^2\mathbf{R} e^{i\mathbf{q}\cdot\mathbf{R}} V(\mathbf{r}, \mathbf{R}) \chi_f^\dagger(\mathbf{r}) \chi_i(\mathbf{r}) \right|^2, \quad (2)$$

where $\mathbf{q} = \mathbf{k}_i - \mathbf{k}_f$ is the difference between the initial and final relative momentum of the system, $\chi_{i/f}$ represent the initial/final exciton wave functions, and $V(\mathbf{r}, \mathbf{R})$ represents the interaction potential between the free carrier and the exciton. In Equation (2), \mathbf{r} is the relative position vector of the electron and the hole in the exciton, and \mathbf{R} is the relative position vector from the free carrier to the center of mass of the exciton.

The interaction potential between the free carrier and the exciton in the central field approximation [38] will be modeled by the Rytova–Keldysh potential [42,43], usually employed to describe excitonic phenomena in mono- and few-layer materials and obtained by solving the Poisson equation for a charge embedded in a thin film of vanishing thickness. In real space, the Rytova–Keldysh potential is given by

$$V_{RK}(\mathbf{r}) = \frac{\hbar c \alpha}{\epsilon} \frac{\pi}{2r_0} \left[H_0\left(\epsilon \frac{r}{r_0}\right) - Y_0\left(\epsilon \frac{r}{r_0}\right) \right], \quad (3)$$

where $\alpha = 1/137$ is the fine-structure constant, ϵ is the mean dielectric constant of the medium above/below the layered material, $H_0(x)$ is the zeroth-order Struve function, and $Y_0(x)$ is the zeroth-order Bessel function of the second kind. The parameter r_0 corresponds to an in-plane screening length related to the 2D polarizability of the material and can be calculated from the single particle Hamiltonian of the system [44]. Additional contributions to this screening length can also originate from the 2D free carriers gas of varying density [45]. In the limit of zero screening length, the Rytova–Keldysh potential becomes the Coulomb potential. Considering again the interaction between the free carrier and the exciton, the interaction potential is

$$V(\mathbf{r}, \mathbf{R}) = \pm [V_{RK}(\mathbf{r}_{ch}) - V_{RK}(\mathbf{r}_{ce})], \tag{4}$$

where \pm distinguishes between the free carrier being a hole (+) or an electron (−), \mathbf{r}_{ch} is the distance between the free carrier and the hole of the exciton, and \mathbf{r}_{ce} is the distance between the free carrier and the electron of the exciton. These two vectors can be written from \mathbf{r} and \mathbf{R} as in [37]

$$\mathbf{r}_{ch} = \mathbf{R} - \frac{\sigma}{1 + \sigma} \mathbf{r}, \quad \mathbf{r}_{ce} = \mathbf{R} + \frac{1}{1 + \sigma} \mathbf{r}, \tag{5}$$

where $\sigma = m_e / m_h$ is the ratio between the effective electron and hole masses. Returning to the discussion on the scattering cross section from Equation (2), the integration over \mathbf{R} reads

$$\int d^2\mathbf{R} e^{i\mathbf{q}\cdot\mathbf{R}} V(\mathbf{r}, \mathbf{R}) = \pm \left[\int d^2\mathbf{R} e^{i\mathbf{q}\cdot\mathbf{R}} V_{RK}(\mathbf{r}_{ch}) - \int d^2\mathbf{R} e^{i\mathbf{q}\cdot\mathbf{R}} V_{RK}(\mathbf{r}_{ce}) \right], \tag{6}$$

which can be computed directly [41] by performing a change in integration variables back to \mathbf{r}_{ch} , \mathbf{r}_{ce} and reads

$$\pm \left[e^{iq\frac{\sigma}{1+\sigma}r \cos(\phi_r)} - e^{-iq\frac{1}{1+\sigma}r \cos(\phi_r)} \right] 2\pi \frac{\hbar c \alpha}{\epsilon} \frac{1}{q(1+r_0q)}, \tag{7}$$

with ϕ_r as the angle between \mathbf{r} and \mathbf{q} , and

$$V_{RK}(\mathbf{q}) = 2\pi \frac{\hbar c \alpha}{\epsilon} \frac{1}{q(1+r_0q)} \tag{8}$$

the Fourier transform of the Rytova–Keldysh potential. Finally, the differential scattering cross section can be written as

$$I_{fi}(\theta) = \frac{M^2}{2\pi\hbar^4 k_i} \left| 2\pi \frac{\hbar c \alpha}{\epsilon} \frac{1}{q(1+r_0q)} J(i \rightarrow f) \right|^2. \tag{9}$$

with the dependence on the initial and final exciton states included in $J(i \rightarrow f)$, defined as

$$J(i \rightarrow f) = \int_0^{+\infty} r dr \int_0^{2\pi} d\phi_r \left[e^{i\frac{\sigma}{1+\sigma}qr \cos\phi_r} - e^{-i\frac{1}{1+\sigma}qr \cos\phi_r} \right] \chi_f^\dagger(\mathbf{r}) \chi_i(\mathbf{r}). \tag{10}$$

3. Total Cross Section

Knowing the differential cross section given by Equation (9), we can now compute the full scattering cross section. To this effect, we must simply perform an angular integration in θ as

$$Q_{i \rightarrow f} = \int_{-\pi}^{\pi} d\theta I_{i \rightarrow f}(\theta) \tag{11}$$

and, explicitly substituting Equation (9), the full cross section is given by

$$Q_{i \rightarrow f}(k_i) = \frac{2\pi M^2 (\hbar c \alpha)^2}{\hbar^4 \epsilon^2 k_i} \int_{-\pi}^{\pi} d\theta \left| \frac{J(i \rightarrow f)}{q(1+r_0q)} \right|^2. \tag{12}$$

To compute this integral, however, we must first define the exciton wave functions, which we will consider when computing Equation (10). We must also define the type of scattering in question, as it will introduce both the specific θ dependence in \mathbf{q} as well as specific thresholds for the relative momentum of the free carrier–exciton system from conservation of energy.

3.1. Elastic Scattering

In an elastic scattering process, the exciton remains in its ground state after the collision, meaning $|\mathbf{k}_i| = |\mathbf{k}_f|$. As such, we can write

$$q = 2 \left| \sin\left(\frac{\theta}{2}\right) \right| k_i. \tag{13}$$

Additionally, we also have $\chi_{f,i}(\mathbf{r}) = \chi_{1s}(r)$, where we consider a simple variational *ansatz* [46,47] based on the eigenfunctions of the two-dimensional hydrogen atom [48,49] and given by

$$\chi_{1s}(r) = \mathcal{N}_{1s} e^{-r\gamma_{1s}/2}, \tag{14}$$

with \mathcal{N}_{1s} a normalization constant given by

$$\mathcal{N}_{1s} = \left[\int r dr d\theta \left(e^{-r\gamma_{1s}/2} \right)^2 \right]^{-1/2} = \frac{\gamma_{1s}}{\sqrt{2\pi}} \tag{15}$$

and γ_{1s} a variational parameter. This variational parameter is computed by minimization of the energy expectation value of the Wannier Equation [50]

$$H = -\frac{\hbar^2 c^2}{2\mu} \nabla^2 + V_{RK}(\mathbf{r}), \tag{16}$$

with $V_{RK}(\mathbf{r})$ the Rytova–Keldysh potential.

With this *ansatz*, we can directly substitute the wave function into $J(i \rightarrow f)$, given by Equation (10), and obtain

$$J_{\text{elast}}(q) = J(1s \rightarrow 1s) = \gamma_{1s}^3 \left[\frac{1}{\left[\left(\frac{\sigma}{1+\sigma} q \right)^2 + \gamma_{1s}^2 \right]^{3/2}} - \frac{1}{\left[\left(\frac{1}{1+\sigma} q \right)^2 + \gamma_{1s}^2 \right]^{3/2}} \right] \tag{17}$$

after integration. This is then substituted into Equation (12), reading

$$Q_{\text{elast}}(k_i) = \frac{2\pi M^2 (\hbar c \alpha)^2}{\hbar^4 \epsilon^2 k_i} \int_{-\pi}^{\pi} d\theta \left| \frac{J_{\text{elast}}(q)}{q(1+r_0q)} \right|^2, \tag{18}$$

where q is given by Equation (13). This integral has no analytical solution and must be computed numerically.

To finalize the computation of the elastic cross section, we must choose a set of material specific parameters. We consider those corresponding to monolayer hexagonal boron–nitride (hBN) encapsulated in fused quartz, with dielectric constant $\epsilon = 3.8$ [51]. The electron and hole masses in this material are $m_e = 0.83 m_0$, $m_h = 0.63 m_0$ [52], with m_0 the electron rest mass, and screening length $r_0 = 10 \text{ \AA}$ [53]. This material was chosen, as both the screening length and the electron/hole masses are known accurately. The obtained variational energy for the 1s excitonic state is $E_{1s} = -58.9 \text{ meV}$.

Varying the initial relative wave vector, we obtain the plot of the total elastic cross section from Equation (12) in Figure 1. We can see that the cross section for electron scattering is always larger than that for hole scattering, as expected from the fact that the reduced mass of the system is larger when the free carrier considered is an electron. A very quick increase from zero relative momentum up to a global maximum is also observed, consistent with the results of Feng and Spector [41] for elastic scattering.

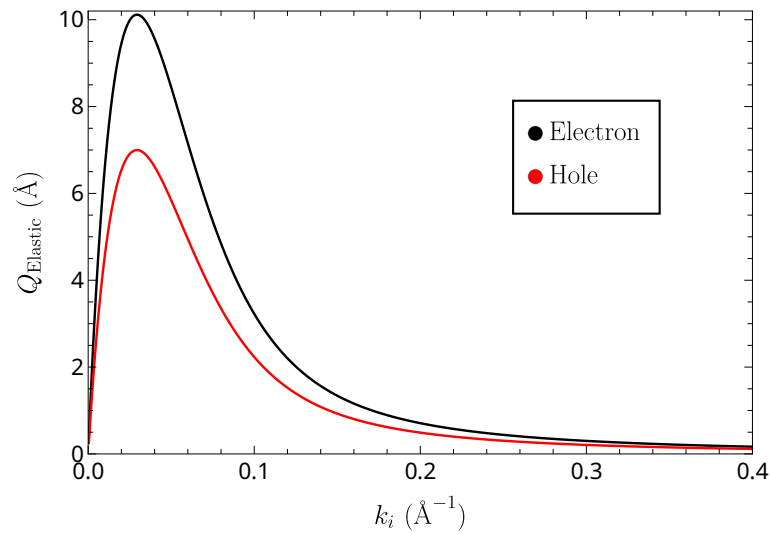


Figure 1. Total elastic cross section for electron–exciton (black) and hole–exciton (red) scattering in hBN encapsulated in fused quartz as a function of the initial relative wave vector.

3.2. Inelastic Scattering

Let us now consider inelastic scattering between free carriers and the exciton. The relative momenta is now given by

$$q^2 = k_f^2 + k_i^2 - 2k_i k_f \cos(\theta), \tag{19}$$

with k_f obtained from the conservation of energy as

$$k_f^2 = k_i^2 - \frac{2M}{\hbar^2}(E_f - E_i). \tag{20}$$

Here, $E_{f/i}$ is the energy of the final/initial state of the exciton, respectively. Substituting this relation into Equation (19), we obtain

$$q^2 = 2k_i^2 - \frac{2M}{\hbar^2}\Delta_{f,i} - 2k_i^2 \sqrt{1 - \frac{2M}{\hbar^2} \frac{\Delta_{f,i}}{k_i^2}} \cos(\theta), \tag{21}$$

with $\Delta_{f,i} = E_f - E_i$. A threshold in k_i below which no scattering is allowed, is immediately evident, obtained from Equation (21) as

$$k_{\min} = \sqrt{\frac{2M}{\hbar^2}(E_f - E_i)}. \tag{22}$$

Below this threshold, there is not enough energy in the scattering process to allow the jump between excitonic states $i \rightarrow f$.

Besides knowing the energies of the final states, we must also know their wave functions. These are obtained [46–48] in a similar form to Equation (14) and are given by

$$\chi_{2s}(r) = \mathcal{N}_{2s} \left(1 - \frac{r}{d}\right) e^{-r\gamma_{2s}/2}, \quad \chi_{2p\pm}(r) = \mathcal{N}_{2p} r e^{\pm i\theta} e^{-r\gamma_{2p}/2}, \tag{23}$$

where γ_{2s}, γ_{2p} are variational parameters, $\mathcal{N}_{2s}, \mathcal{N}_{2p}$ are normalization constants given by

$$\mathcal{N}_{2s} = \frac{2\gamma_{2s}^2}{\sqrt{\pi} \sqrt{3\gamma_{1s}^2 - 2\gamma_{1s}\gamma_{2s} + 3\gamma_{2s}^2}}, \quad \mathcal{N}_{2p} = \frac{\gamma_{2p}^2}{2\sqrt{3\pi}}, \tag{24}$$

and d is a parameter obtained by imposing orthogonality between χ_{1s} and χ_{2s} , given by

$$d = \frac{4}{\gamma_{1s} + \gamma_{2s}}. \tag{25}$$

These wave functions, together with the 1s wave function, are plotted in Figure 2 for monolayer hBN encapsulated in fused quartz.

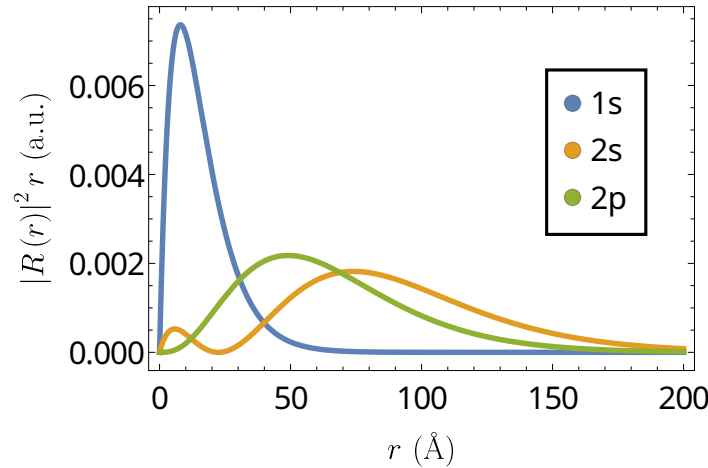


Figure 2. Radial probability density for the 1s (blue), 2s (orange), and 2p (green) states as described by the variational wave functions of Equations (14) and (23) in a hBN monolayer encapsulated in fused quartz.

3.2.1. 1s → 2s Transitions

We will first consider 1s → 2s transitions. To compute $J_{2s} = J(1s \rightarrow 2s)$, we recall Equation (10) and, after integration, obtain

$$J_{2s} = \frac{3\gamma_{1s}(\gamma_{1s} + \gamma_{2s})\gamma_{2s}^2}{\sqrt{6\gamma_{1s}^2 - 4\gamma_{1s}\gamma_{2s} + 6\gamma_{2s}^2}} \left[\frac{q^2 \left(\frac{\sigma}{1+\sigma}\right)^2}{\left[q^2 \left(\frac{\sigma}{1+\sigma}\right)^2 + \left(\frac{\gamma_{1s} + \gamma_{2s}}{2}\right)^2 \right]^{5/2}} - \frac{q^2 \left(\frac{1}{1+\sigma}\right)^2}{\left[q^2 \left(\frac{1}{1+\sigma}\right)^2 + \left(\frac{\gamma_{1s} + \gamma_{2s}}{2}\right)^2 \right]^{5/2}} \right],$$

where q is obtained from Equation (21) as

$$q^2 = 2k_i^2 - \frac{2M}{\hbar^2} \Delta_{2s,1s} - 2k_i^2 \sqrt{1 - \frac{2M}{\hbar^2} \frac{\Delta_{2s,1s}}{k_i^2} \cos(\theta)}. \tag{26}$$

As discussed above, the energy of the 2s state is obtained by minimization of the Wannier equation with the variational wave functions, and its value is $E_{2s} = -8.83$ meV for our system. Explicitly computing the thresholds from Equation (22), we obtain $k_{\min} = 0.0833 \text{ \AA}^{-1}$ for electron–exciton scattering and $k_{\min} = 0.0760 \text{ \AA}^{-1}$ for hole–exciton scattering.

3.2.2. 1s → 2p Transitions

For computing $J(1s \rightarrow 2p_{\pm})$ following Equation (10), we must consider the distinction between p_{\pm} states. This is, however, not important, as the two states are degenerate, and the two integrals $J(1s \rightarrow 2p_{+})$, $J(1s \rightarrow 2p_{-})$ are, in fact, equal. As such, we take into account the two 2p states by multiplying the total cross section by an angular momentum degeneracy factor $g_{\ell} = 2$.

Explicitly, $J_{2p} = J(1s \rightarrow 2p)$ is given by

$$J_{2p} = \frac{3\gamma_{1s}\gamma_{2p}^2(\gamma_{1s} + \gamma_{2p})}{2\sqrt{6}} \left[\frac{iq \frac{\sigma}{1+\sigma}}{\left[q^2 \left(\frac{\sigma}{1+\sigma}\right)^2 + \left(\frac{\gamma_{1s} + \gamma_{2p}}{2}\right)^2 \right]^{5/2}} + \frac{iq \frac{1}{1+\sigma}}{\left[q^2 \left(\frac{1}{1+\sigma}\right)^2 + \left(\frac{\gamma_{1s} + \gamma_{2p}}{2}\right)^2 \right]^{5/2}} \right].$$

The relative momentum q is defined analogously to Equation (26), with the only factor missing being the energy of the $2p_{\pm}$ states.

For our system, this energy is $E_{2p} = -10.2$ meV. As such, the thresholds from Equation (22) are now $k_{\min} = 0.0822 \text{ \AA}^{-1}$ for electron–exciton scattering and $k_{\min} = 0.0749 \text{ \AA}^{-1}$ for hole–exciton scattering.

3.3. Joint Elastic and Inelastic Scattering

Finally, we consider the joint contribution to the scattering cross section from both elastic and inelastic scattering. This cross section will, therefore, involve a sum over final states, where only the $1s \rightarrow 1s$ contribution originates from elastic scattering processes. Explicitly, and for an arbitrary set of final exciton states f , the total scattering cross section is given by

$$Q_{\text{Total}} = \sum_f Q_{1s \rightarrow f}. \tag{27}$$

For the three transitions discussed previously, the sum in Equation (27) is restricted and is explicitly written as

$$Q_{\text{Total}} = Q_{1s \rightarrow 1s} + Q_{1s \rightarrow 2s} + Q_{1s \rightarrow 2p}. \tag{28}$$

This total scattering cross section is plotted in Figure 3 for both types of free carriers, together with the dashed lines representing the thresholds for the inelastic scattering processes considered.

Analyzing Figure 3, we can see that, when the same scattering process is allowed for both types of free carriers, electron–exciton scattering has a cross section roughly $1.5 \times$ larger. This trend is, however, inverted between the threshold momentum for hole–exciton $1s \rightarrow 2p$ scattering, and the threshold momentum for electron–exciton $1s \rightarrow 2p$, i.e., between $k_i = 0.0749 \text{ \AA}^{-1}$ and $k_i = 0.0822 \text{ \AA}^{-1}$. In this momentum range, the dominant $1s \rightarrow 2p$ process is already allowed for hole–exciton scattering, leading to a vastly superior cross section relative to that for electron–exciton scattering.

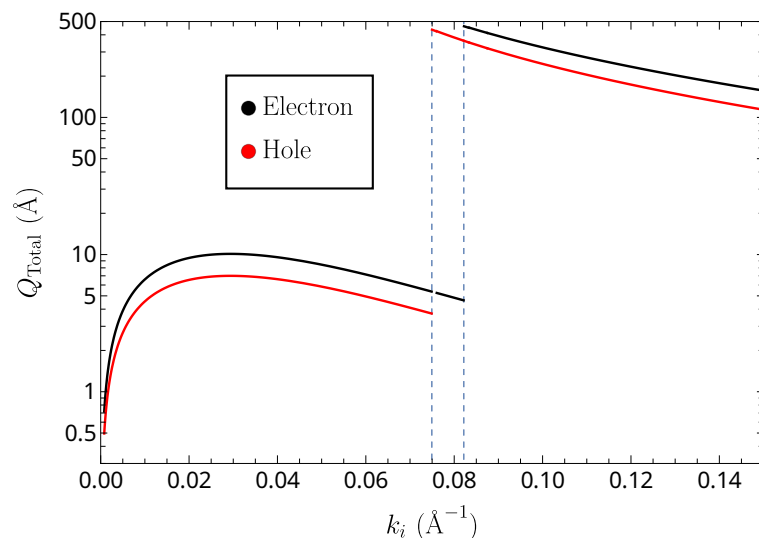


Figure 3. Total cross section for electron–exciton (black) and hole–exciton (red) scattering in hBN encapsulated in fused quartz as a function of the initial relative wave vector. Vertical dashed lines represent the electron–exciton and hole–exciton scattering thresholds for the $1s \rightarrow 2p$ transition, located at $k_{\min,e^-} = 0.0822 \text{ \AA}^{-1}$ and $k_{\min,h} = 0.0749 \text{ \AA}^{-1}$.

The final threshold included, visible in Figure 3 as the dashed purple lines, originates from $1s \rightarrow 3d$ scattering, as $E_{3d} = -3.74$ meV is the lowest energy state after $2s$. These take place at $k_{\min} = 0.0875 \text{ \AA}^{-1}$ for electron–exciton scattering and $k_{\min} = 0.0798 \text{ \AA}^{-1}$ for

hole–exciton scattering. These are, however, much smaller than the peaks in Figure 3, similar to what was observed in Ref. [37], and are invisible in Figure 3.

4. Scattering Contribution to Exciton Linewidth

To conclude our study of the scattering of excitons with free carriers in layered materials, we will now discuss the contribution from these scattering processes to the excitonic linewidth. This will provide a point of comparison against experimental studies [54]. Although other phenomena will also contribute to this linewidth, such as radiative lifetimes [27] and phonon scattering [25], the dependence of the free carrier scattering on both temperature and carrier density should provide a good distinction of the various contributing processes. As hBN is a large bandgap insulator, carrier doping in this material is usually performed chemically by diluting impurities [55–58].

The contribution to the excitonic linewidth from free carrier scattering is given by [24,59–61]

$$\Gamma_{\text{Total}} = \sum_f \frac{2\hbar^2}{\pi M} \int_0^\infty dk k^2 f \left(\frac{m_c + m_e + m_h}{m_e + m_h} k \right) Q_{1s \rightarrow f}, \quad (29)$$

where $Q_{1s \rightarrow f}$ is, as described earlier, the scattering cross section associated with a specific transition from the excitonic ground state to a final state f . As we are summing over final states f , and only $Q_{1s \rightarrow f}$ depends on the final state, this is equivalent to switching the sum over final states and the integral and writing

$$\Gamma_{\text{Total}} = \frac{2\hbar^2}{\pi M} \int_0^\infty dk k^2 n_F \left(\frac{m_c + m_e + m_h}{m_e + m_h} k \right) Q_{\text{Total}}, \quad (30)$$

where Q_{Total} is the total scattering cross section as plotted in Figure 3. Here, $n_F(k)$ is the Fermi–Dirac distribution for free carriers, given by

$$n_F(k) = \frac{1}{e^{\frac{E_k - E_F}{k_B T}} + 1} \quad (31)$$

where the dispersion relation is given by

$$E_k = \frac{\hbar^2}{2m_c} k^2 \quad (32)$$

and the Fermi energy is

$$E_F = 2\pi \frac{\hbar^2}{2m_c} n, \quad (33)$$

with n the area density of free carriers. We consider carrier densities up to a maximum of 10^{12} cm^{-2} , where the average separation of free carriers $d_c = 2(\pi n)^{-1/2}$ is still larger but already of the order of the root mean square (RMS) exciton radius, given by

$$r_{\text{RMS};n} = \int_0^\infty \int_0^{2\pi} r dr d\theta \psi_n(r, \theta)^\dagger r^2 \psi_n(r, \theta). \quad (34)$$

For the two excitonic states most relevant to the scattering cross section, $1s$ and $2p$, the RMS exciton radius is $r_{\text{RMS};1s} = 19.5 \text{ \AA}$ and $r_{\text{RMS};2p} = 73.2 \text{ \AA}$, respectively, while the average separation between free carriers is $d_c = 113 \text{ \AA}$.

As before, we must compute the integral of Equation (30) numerically. The specific methodology for the discretization of Equation (30) is discussed in Appendix B. Choosing a Gauss–Legendre quadrature [62] of size $N = 450$, the results for the contribution of scattering with free carriers to the excitonic linewidth are presented in Figure 4 as a function of temperature for free carrier area densities of $n = 10^9 \text{ cm}^{-2}$ and $n = 10^{12} \text{ cm}^{-2}$. In Figure 5, we present the excitonic linewidth as a function of the free carrier area density

for four distinct values of the temperature T between 10 K and 300 K. As expected, the excitonic linewidth contribution increases with both temperature and carrier density as these phenomena increase the kinetic energy of the carriers and their proximity, respectively.

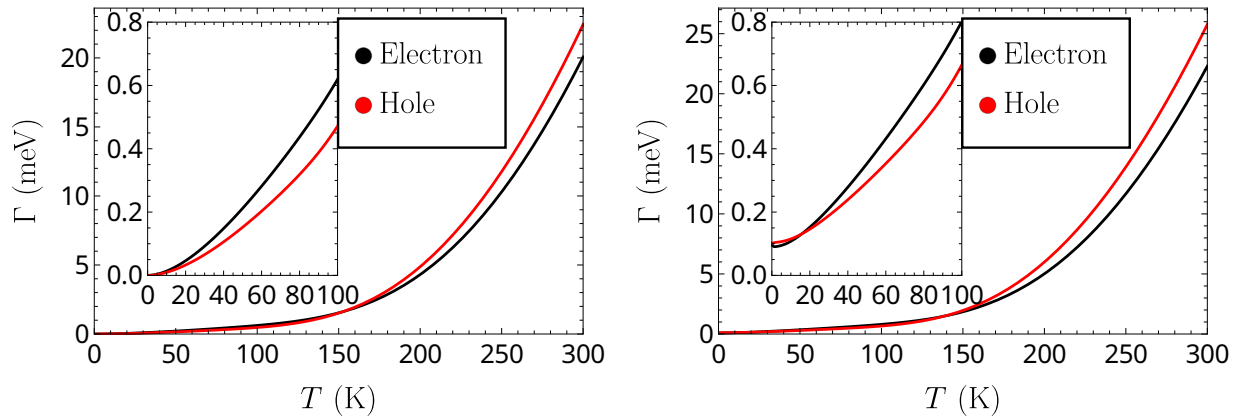


Figure 4. Contribution to exciton linewidth from scattering with free carriers as a function of the temperature at constant free carrier area density $n = 10^9 \text{ cm}^{-2}$ (left) and $n = 10^{12} \text{ cm}^{-2}$ (right). Insets show the low-temperature region of the plot for clarity.

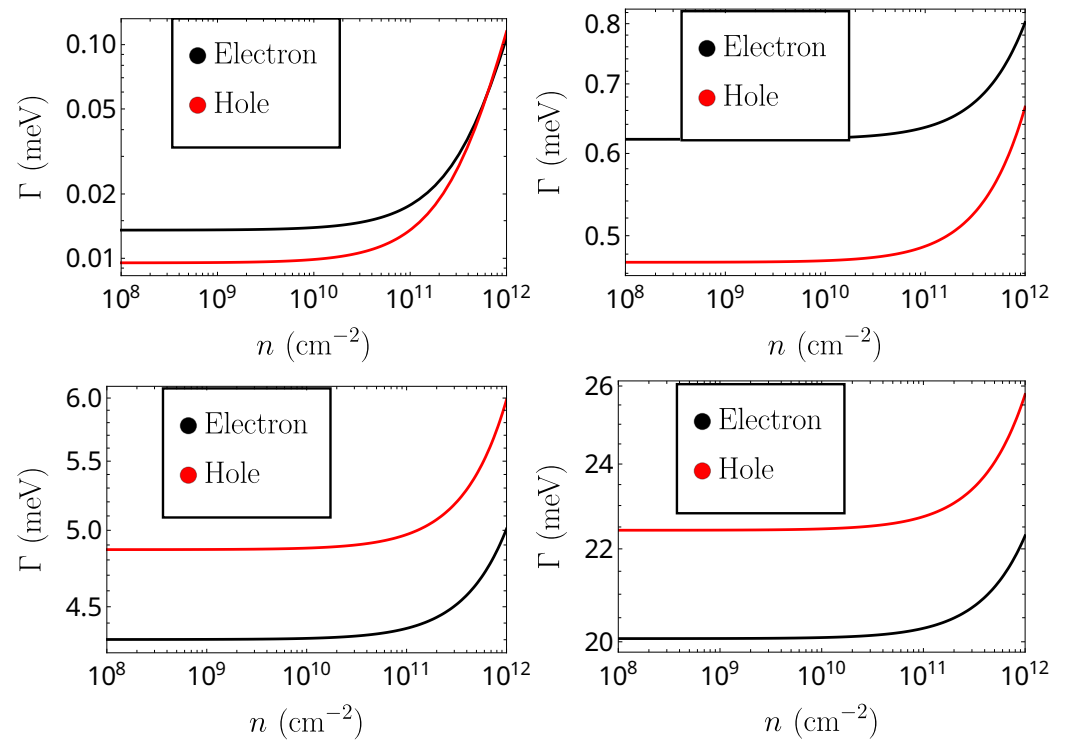


Figure 5. Contribution to exciton linewidth from scattering with free carriers as a function of the free carrier area density at constant temperature $T = 10 \text{ K}$ (top-left), $T = 100 \text{ K}$ (top-right), $T = 200 \text{ K}$ (bottom-left), and $T = 300 \text{ K}$ (bottom-right).

5. Conclusions

In this paper, we studied the effects of scattering between free carriers and excitons in monolayer materials and its contribution to the excitonic linewidth. To this end, we began by reviewing the general form of the expressions for the differential cross section between free carriers and excitons in two dimensions [37], as well as the inclusion of screening in the differential cross section. Briefly reviewing the computation of variational functions for the exciton wave functions, we discussed both elastic and inelastic scattering processes.

While elastic scattering was the sole contributor to the scattering cross section for low relative momentum, inelastic $1s \rightarrow 2p$ scattering dominated the total cross section when allowed by conservation of energy. This dominant scattering had a maximum cross section roughly 40 times larger than that of elastic scattering, as seen in Figure 3. Considering inelastic scattering processes to higher energy states, namely $2s$ and $3d$, their amplitude was negligible when compared to the dominant process (roughly 400 times smaller). This dominant behavior of $1s \rightarrow 2p$ transitions was very similar to what was presented in Figures 2 and 9 of Ref. [37], although the specific ratios were highly dependent on the electron and hole masses.

After discussing the relation between the total scattering cross section and the excitonic linewidth, we considered its dependence on both temperature and free carrier density. First, looking at the exciton linewidth for reasonable values of the carrier density in layered materials [63–65], namely 10^9 cm^{-2} and 10^{12} cm^{-2} , we observed that the difference in linewidth between the two regimes was clearly noticeable as the linewidth became finite at $T = 0 \text{ K}$ for larger carrier densities. Additionally, the contribution from exciton–hole scattering became larger than that of electron–exciton scattering slightly earlier at a higher carrier density, namely at $T \gtrsim 150 \text{ K}$ for $n = 10^9 \text{ cm}^{-2}$ and at $T \approx 140 \text{ K}$ for $n = 10^{12} \text{ cm}^{-2}$. Further increasing the carrier density to values above 10^{13} cm^{-2} would produce even greater differences. These higher carrier densities would already imply an average free carrier separation d_c much smaller than the RMS exciton radius for the $2p$ excitonic state, which would make more complex excitonic phenomena, such as biexcitons and trions [66–69], increasingly significant.

Regarding the excitonic linewidth at fixed temperatures, the free carrier scattering contribution remained in the 0.5–20 meV range for temperatures between 100 and 300 K. For temperatures in this range, the computed linewidth remained essentially constant at a temperature-dependent value as the carrier density increased until roughly $n \approx 10^{11} \text{ cm}^{-2}$. Past $n \approx 10^{11} \text{ cm}^{-2}$, the computed linewidth rapidly increased for all values of the temperature, although the growth occurred sooner and faster for lower temperatures, as can be seen in the top-left plot of Figure 5 for $T = 10 \text{ K}$.

From these results, it should be feasible to measure the free-carrier scattering contribution to the excitonic linewidth, as good quality samples of both hBN and transition metal dichalcogenides have been grown in the past that presented excitonic linewidths in this order of magnitude [11–15].

Author Contributions: Formal analysis, M.F.C.M.Q.; Supervision, N.M.R.P.; Writing—original draft, M.F.C.M.Q.; Writing—review & editing, N.M.R.P. All authors have read and agreed to the published version of the manuscript.

Funding: M.F.C.M.Q. acknowledges the International Nanotechnology Laboratory (INL) and the Portuguese Foundation for Science and Technology (FCT) for the Quantum Portugal Initiative (QPI) grant SFRH/BD/151114/2021. N.M.R.P. acknowledges support by the Portuguese Foundation for Science and Technology (FCT) in the framework of the Strategic Funding UIDB/04650/2020, COMPETE 2020, PORTUGAL 2020, FEDER, and FCT through projects PTDC/FIS-MAC/2045/2021, EXPL/FIS-MAC/0953/2021, and from the European Commission through the project Graphene Driven Revolutions in ICT and Beyond (Ref. No. 881603, CORE 3).

Institutional Review Board Statement: Not applicable.

Informed Consent Statement: Not applicable.

Data Availability Statement: Not applicable.

Conflicts of Interest: The authors declare no conflict of interest.

Abbreviations

The following abbreviations are used in this manuscript:

hBN hexagonal boron nitride
RMS root mean squared

Appendix A. Derivation of Differential Scattering Cross Section

For the derivation of the differential scattering cross section of Equation (2), we follow closely the derivation performed by Feng and Spector [41]. We consider an encounter between two bodies *A* (free carrier) and *B* (exciton), which are in their ground state prior to the collision. The reduced mass of this system is $M = \frac{m_A m_B}{m_A + m_B}$. Prior to the collision, the internal motions of each of the two bodies are given by their independent Hamiltonians

$$H_A \chi_{A,n}(\mathbf{r}_A) = E_{A,n} \chi_{A,n}(\mathbf{r}_A), \quad H_B \chi_{B,m}(\mathbf{r}_B) = E_{B,m} \chi_{B,m}(\mathbf{r}_B), \quad (A1)$$

where $\chi_{A,n}/\chi_{B,m}$ are the independent wave functions for the internal motion of the two bodies *A/B* in the states *n/m*, respectively, and $E_{A,n}/E_{B,m}$ their energies. In the absence of the interaction of the two bodies, their relative motion is given by

$$\left[-\frac{\hbar^2}{2M} \nabla^2 - \frac{1}{2} M \mathbf{v}^2 \right] F_{11}(\mathbf{R}) = 0, \quad (A2)$$

with \mathbf{v} and \mathbf{R} the relative velocity and position of the two particles and $F_{11}(\mathbf{R})$ the part of the wave function related to the relative motion of the particles in their ground state.

The complete wave equation for this system is given by

$$\left[-\frac{\hbar^2}{2M} \nabla^2 - \frac{1}{2} M \mathbf{v}^2 + H_A - E_{A,1} + H_B - E_{B,1} + V(\mathbf{R}, \mathbf{r}_A, \mathbf{r}_B) \right] \Psi(\mathbf{R}, \mathbf{r}_A, \mathbf{r}_B) = 0, \quad (A3)$$

where $V(\mathbf{R}, \mathbf{r}_A, \mathbf{r}_B)$ is the interaction potential between the two particles. The wave function can then be expanded in terms of the basis functions $\chi_{A,n}/\chi_{B,m}$, reading

$$\Psi(\mathbf{R}, \mathbf{r}_A, \mathbf{r}_B) = \sum_{n,m} F_{nm}(\mathbf{R}) \chi_{A,n}(\mathbf{r}_A) \chi_{B,m}(\mathbf{r}_B), \quad (A4)$$

meaning that $F_{nm}(\mathbf{R})$ must obey

$$\left[\nabla^2 + k^2 \right] F_{nm}(\mathbf{R}) = \frac{2M}{\hbar^2} \int d\mathbf{r}_A d\mathbf{r}_B V(\mathbf{r}_A, \mathbf{r}_B, \mathbf{R}) \Psi(\mathbf{r}_A, \mathbf{r}_B, \mathbf{R}) \chi_{A,n}^*(\mathbf{r}_A) \chi_{B,m}^*(\mathbf{r}_B), \quad (A5)$$

where

$$\mathbf{k}^2 = \frac{2M}{\hbar^2} \left[\frac{1}{2} M \mathbf{v}^2 + E_{A,1} - E_{A,n} + E_{B,1} - E_{B,m} \right]. \quad (A6)$$

The relation in Equation (A6) immediately leads to the thresholds for inelastic scattering, as k being real implies $\frac{1}{2} M \mathbf{v}^2 > E_{A,n} - E_{A,1} + E_{B,m} - E_{B,1}$.

The solution to Equation (A5) reads

$$F_{nm}(\mathbf{R}) = \frac{-iM}{2\hbar^2} \int d\mathbf{r}_A d\mathbf{r}_B d\mathbf{R}' V(\mathbf{r}_A, \mathbf{r}_B, \mathbf{R}') \Psi(\mathbf{R}', \mathbf{r}_A, \mathbf{r}_B) \chi_{A,n}^*(\mathbf{r}_A) \chi_{B,m}^*(\mathbf{r}_B) H_0^1(k|\mathbf{R} - \mathbf{R}'|), \quad (A7)$$

where $H_0^1(k|\mathbf{R} - \mathbf{R}'|)$ is the Hankel function of the first kind, which is the solution to Equation (A2). This function satisfies the boundary condition that, for $\mathbf{R} \gg \mathbf{R}'$, the solution represents an outgoing circular wave.

Following an identical procedure to that which is used to apply the Born approximation in a 3D system, the asymptotic regime as $\mathbf{R} \rightarrow \infty$ for $F_{nm}(\mathbf{R})$ reads

$$F_{nm}(\mathbf{R}) \rightarrow e^{i\mathbf{k}_0 \cdot \mathbf{R}} + \frac{e^{i\mathbf{k} \cdot \mathbf{R}}}{\sqrt{\mathbf{R}}} f_{nm}(\theta), \quad (A8)$$

where it was assumed that the asymptotic form of the solution is the sum of an incoming plane wave and an outgoing circular wave. In Equation (A8), \mathbf{k}_0/\mathbf{k} are the initial/final wave vectors for the scattered particles, respectively, and

$$f_{nm}(\theta) = -\frac{Me^{i\pi/4}}{\sqrt{2\pi k\hbar^2}} \int d\mathbf{r}_A d\mathbf{r}_B d\mathbf{R}' e^{i(\mathbf{k}_0 - \mathbf{k}) \cdot \mathbf{R}'} V(\mathbf{r}_A, \mathbf{r}_B, \mathbf{R}') \chi_{A,n}^*(\mathbf{r}_A) \chi_{A,1}(\mathbf{r}_A) \chi_{B,m}^*(\mathbf{r}_B) \chi_{B,1}(\mathbf{r}_B). \quad (\text{A9})$$

The 2D differential scattering cross section is, analogously to that of a 3D system, given by [41]

$$I_{n,m}(\theta) = \frac{k}{k_0} |f_{nm}(\theta)|^2 = \frac{M^2}{2\pi k_0 \hbar^4} \left| \int d\mathbf{r}_A d\mathbf{r}_B d\mathbf{R}' e^{i\mathbf{q} \cdot \mathbf{R}'} V(\mathbf{r}_A, \mathbf{r}_B, \mathbf{R}') \chi_{A,n}^*(\mathbf{r}_A) \chi_{A,1}(\mathbf{r}_A) \chi_{B,m}^*(\mathbf{r}_B) \chi_{B,1}(\mathbf{r}_B) \right|^2, \quad (\text{A10})$$

with $\mathbf{q} = \mathbf{k}_0 - \mathbf{k}$. Finally, recalling that the free carrier (electron or hole) has no internal structure, the sum of the internal energies of the system reduces to that of the exciton. Furthermore, Equation (A10) can be simplified further by assuming a central field approximation, reading

$$I_{n,m}(\theta) = \frac{M^2}{2\pi k_0 \hbar^4} \left| \int d\mathbf{r} d\mathbf{R}' e^{i\mathbf{q} \cdot \mathbf{R}'} V(\mathbf{r}, \mathbf{R}') \chi_n^*(\mathbf{r}) \chi_1(\mathbf{r}) \right|^2, \quad (\text{A11})$$

where χ is now the wave function of the exciton, \mathbf{r} is the relative position of the electron and hole in the exciton, and \mathbf{R}' is the relative position from the free carrier to the center of mass of the exciton.

Appendix B. Computation of Scattering Contribution to Excitonic Linewidth

We begin by changing the integration limits $[0, +\infty)$ to a finite limit, in this case $[0, 1]$, via a change in variables defined as $k = \tan\left(\frac{\pi x}{2}\right)$. With this change in variables, the integral of Equation (30) reads

$$\Gamma_{\text{Total}} = \frac{2\hbar^2}{\pi M} \int_0^1 dx \frac{dk}{dx} k(x)^2 n_F\left(\frac{m_c + m_e + m_h}{m_e + m_h} k(x)\right) Q_{\text{Total}}(k(x)). \quad (\text{A12})$$

We can then define a grid of points x_i for our discretization, meaning that

$$\Gamma_{\text{Total}} = \frac{2\hbar^2}{\pi M} \sum_{i=1}^N w_i \frac{dk}{dx_i} k_i^2 n_F\left(\frac{m_c + m_e + m_h}{m_e + m_h} k_i\right) Q_{\text{Total}}(k_i), \quad (\text{A13})$$

where N is the number of points considered in the discretization, w_i is the weight function of the quadrature in question, and the discretized variables are defined as $q_i \equiv q(x_i)$, and $\frac{dk}{dx_i} \equiv \frac{dk}{dx} \Big|_{x=x_i}$. For the numerical quadrature, we employ a Gauss–Legendre quadrature [62], defined as

$$\int_a^b f(x) dx \approx \sum_{i=1}^N f(x_i) w_i,$$

where

$$x_i = \frac{a + b + (b - a)\zeta_i}{2}, \quad w_i = \frac{b - a}{(1 - \zeta_i^2) \left[\frac{dP_N(x)}{dx} \Big|_{x=\zeta_i} \right]^2},$$

with ζ_i the i -th zero of the Legendre polynomial $P_N(x)$.

References

1. Àla Guillaume, C.B.; Debever, J.M.; Salvan, F. Radiative Recombination in Highly Excited CdS. *Phys. Rev.* **1969**, *177*, 567–580. [CrossRef]
2. Iwai, S.; Namba, S. Emission Spectra in CdS under High Excitation by Electron Beam. *Appl. Phys. Lett.* **1971**, *19*, 41–43. [CrossRef]

3. In Yu, C.; Goto, T.; Ueta, M. Emission of Cuprous Halide Crystals at High Density Excitation. *J. Phys. Soc. Jpn.* **1973**, *34*, 693–698. [[CrossRef](#)]
4. Braun, W.; Bille, J.; Fischer, T.; Huber, G. Laser Emission in CdSe Due to Exciton—Exciton and Exciton—Electron Interaction. *Phys. Status Solidi (B)* **1973**, *58*, 759–765. [[CrossRef](#)]
5. Levy, R.; Grun, J.B. Optical properties of strongly excited direct band gap materials. *Phys. Status Solidi (A)* **1974**, *22*, 11–38. [[CrossRef](#)]
6. Klingshirn, C. The Luminescence of ZnO under High One- and Two-Quantum Excitation. *Phys. Status Solidi (B)* **1975**, *71*, 547–556. [[CrossRef](#)]
7. Hönerlage, B.; Klingshirn, C.; Grun, J.B. Spontaneous emission due to exciton—Electron scattering in semiconductors. *Phys. Status Solidi (B)* **1976**, *78*, 599–608. [[CrossRef](#)]
8. Levy, R.; Grun, J.B.; Nikitine, S. Experimental investigation of the competition of stimulated emissions involving exciton. *Excit. High Density* **1975**, *73*, 211–219.
9. Elkomoss, S.G.; Munsch, G. Electron-exciton elastic scattering cross sections in the central field and the exchange approximations. *J. Phys. Chem. Solids* **1977**, *38*, 557–563. [[CrossRef](#)]
10. Elkomoss, S.G.; Munsch, G. Electron-exciton inelastic collision cross sections for different semiconductors. *J. Phys. Chem. Solids* **1979**, *40*, 431–438. [[CrossRef](#)]
11. Reynolds, D.C.; Bajaj, K.K.; Litton, C.W.; Singh, J.; Yu, P.W.; Pearah, P.; Klem, J.; Morkoc, H. High-resolution photoluminescence and reflection studies of GaAs-Al_xGa_{1-x}As multi-quantum-well structures grown by molecular-beam epitaxy: Determination of microscopic structural quality of interfaces. *Phys. Rev. B* **1986**, *33*, 5931–5934. [[CrossRef](#)] [[PubMed](#)]
12. Museur, L.; Feldbach, E.; Kanaev, A. Defect-related photoluminescence of hexagonal boron nitride. *Phys. Rev. B* **2008**, *78*, 155204. [[CrossRef](#)]
13. Cadiz, F.; Courtade, E.; Robert, C.; Wang, G.; Shen, Y.; Cai, H.; Taniguchi, T.; Watanabe, K.; Carrere, H.; Lagarde, D.; et al. Excitonic Linewidth Approaching the Homogeneous Limit in MoS₂-Based van der Waals Heterostructures. *Phys. Rev. X* **2017**, *7*, 021026. [[CrossRef](#)]
14. Elias, C.; Valvin, P.; Pelini, T.; Summerfield, A.; Mellor, C.J.; Cheng, T.S.; Eaves, L.; Foxon, C.T.; Beton, P.H.; Novikov, S.V.; et al. Direct band-gap crossover in epitaxial monolayer boron nitride. *Nat. Commun.* **2019**, *10*, 2639. [[CrossRef](#)] [[PubMed](#)]
15. Li, J.; Wang, J.; Zhang, X.; Elias, C.; Ye, G.; Evans, D.; Eda, G.; Redwing, J.M.; Cassabois, G.; Gil, B.; et al. Hexagonal Boron Nitride Crystal Growth from Iron, a Single Component Flux. *ACS Nano* **2021**, *15*, 7032–7039. [[CrossRef](#)]
16. Vuong, T.Q.P.; Cassabois, G.; Valvin, P.; Rousseau, E.; Summerfield, A.; Mellor, C.J.; Cho, Y.; Cheng, T.S.; Albar, J.D.; Eaves, L.; et al. Deep ultraviolet emission in hexagonal boron nitride grown by high-temperature molecular beam epitaxy. *2D Materials* **2017**, *4*, 021023. [[CrossRef](#)]
17. Kim, S.M.; Hsu, A.; Park, M.H.; Chae, S.H.; Yun, S.J.; Lee, J.S.; Cho, D.H.; Fang, W.; Lee, C.; Palacios, T.; et al. Synthesis of large-area multilayer hexagonal boron nitride for high material performance. *Nat. Commun.* **2015**, *6*, 8662. [[CrossRef](#)]
18. Yano, M.; Yap, Y.K.; Okamoto, M.; Onda, M.; Yoshimura, M.; Mori, Y.; Sasaki, T. Na: A New Flux for Growing Hexagonal Boron Nitride Crystals at Low Temperature. *Jpn. J. Appl. Phys.* **2000**, *39*, L300–L302. [[CrossRef](#)]
19. Dingle, R.; Wiegmann, W.; Henry, C.H. Quantum States of Confined Carriers in Very Thin Al_xGa_{1-x}As-GaAs-Al_xGa_{1-x}As Heterostructures. *Phys. Rev. Lett.* **1974**, *33*, 827–830. [[CrossRef](#)]
20. Miller, D.A.B.; Chemla, D.S.; Eilenberger, D.J.; Smith, P.W.; Gossard, A.C.; Tsang, W.T. Large room-temperature optical nonlinearity in GaAs/Ga_{1-x}Al_xAs multiple quantum well structures. *Appl. Phys. Lett.* **1982**, *41*, 679–681. [[CrossRef](#)]
21. Poellmann, C.; Steinleitner, P.; Leierseder, U.; Nagler, P.; Plechinger, G.; Porer, M.; Bratschitsch, R.; Schüller, C.; Korn, T.; Huber, R. Resonant internal quantum transitions and femtosecond radiative decay of excitons in monolayer WSe₂. *Nat. Mater.* **2015**, *14*, 889–893. [[CrossRef](#)]
22. Merkl, P.; Mooshammer, F.; Steinleitner, P.; Girnghuber, A.; Lin, K.Q.; Nagler, P.; Holler, J.; Schüller, C.; Lupton, J.M.; Korn, T.; et al. Ultrafast transition between exciton phases in van der Waals heterostructures. *Nat. Mater.* **2019**, *18*, 691–696. [[CrossRef](#)] [[PubMed](#)]
23. Lee, J.; Koteles, E.S.; Vassell, M.O. Luminescence linewidths of excitons in GaAs quantum wells below 150 K. *Phys. Rev. B* **1986**, *33*, 5512–5516. [[CrossRef](#)] [[PubMed](#)]
24. Spector, H.N.; Lee, J.; Melman, P. Exciton linewidth in semiconducting quantum-well structures. *Phys. Rev. B* **1986**, *34*, 2554–2560. [[CrossRef](#)]
25. Henriques, J.C.G.; Mortensen, N.A.; Peres, N.M.R. Analytical description of the 1s exciton linewidth temperature dependence in transition metal dichalcogenides. *Phys. Rev. B* **2021**, *103*, 235402. [[CrossRef](#)]
26. Cingolani, R.; Ploog, K. Frequency and density dependent radiative recombination processes in III–V semiconductor quantum wells and superlattices. *Adv. Phys.* **1991**, *40*, 535–623. [[CrossRef](#)]
27. Palummo, M.; Bernardi, M.; Grossman, J.C. Exciton Radiative Lifetimes in Two-Dimensional Transition Metal Dichalcogenides. *Nano Lett.* **2015**, *15*, 2794–2800. [[CrossRef](#)]
28. Singh, J.; Bajaj, K.K. Theory of excitonic photoluminescence linewidth in semiconductor alloys. *Appl. Phys. Lett.* **1984**, *44*, 1075–1077. [[CrossRef](#)]
29. Basu, P.K. Linewidth of free excitons in quantum wells: Contribution by alloy disorder scattering. *Appl. Phys. Lett.* **1990**, *56*, 1110–1112. [[CrossRef](#)]

30. Li, W.; Wang, Z.; Song, A.; Liang, J.; Xu, B.; Zhu, Z.; Zheng, W.; Liao, Q.; Yang, B. Photoluminescence studies on very high-density quasi-two-dimensional electron gases in pseudomorphic modulation-doped quantum wells. *J. Appl. Phys.* **1995**, *78*, 593–595. [[CrossRef](#)]
31. Djurišić, A.B.; Kwok, W.M.; Leung, Y.H.; Chan, W.K.; Phillips, D.L.; Lin, M.S.; Gwo, S. Ultrafast spectroscopy of stimulated emission in single ZnO tetrapod nanowires. *Nanotechnology* **2005**, *17*, 244–249. [[CrossRef](#)]
32. Young, J.F.; Wood, B.M.; Charbonneau, S. Optical Probes of Resonant Tunneling Structures. In *Electronic Properties of Multilayers and Low-Dimensional Semiconductor Structures*; Springer: Boston, MA, USA, 1990; pp. 331–349. [[CrossRef](#)]
33. Teran, F.J.; Martín, M.D.; Calleja, J.M.; Viña, L.; Eaves, L.; Henini, M. Carrier injection effects on exciton dynamics in GaAs/AlAs resonant-tunneling diodes. *EPL (Europhys. Lett.)* **2009**, *85*, 67010. [[CrossRef](#)]
34. Koh, T.S.; Feng, Y.P.; Spector, H.N. Effect of an electric field on the scattering of excitons by free carriers in semiconducting quantum-well structures. *J. Appl. Phys.* **1997**, *81*, 2704–2708. [[CrossRef](#)]
35. Vella, D.; Barbosa, M.B.; Trevisanutto, P.E.; Verzhbitskiy, I.; Zhou, J.Y.; Watanabe, K.; Taniguchi, T.; Kajikawa, K.; Eda, G. In-Plane Field-Driven Excitonic Electro-Optic Modulation in Monolayer Semiconductor. *Adv. Opt. Mater.* **2022**, *10*, 2102132. [[CrossRef](#)]
36. Efimkin, D.K.; Laird, E.K.; Levinsen, J.; Parish, M.M.; MacDonald, A.H. Electron-exciton interactions in the exciton-polaron problem. *Phys. Rev. B* **2021**, *103*, 075417. [[CrossRef](#)]
37. Feng, Y.P.; Spector, H.N. Scattering of excitons by free carriers in semiconducting quantum well structures. *J. Phys. Chem. Solids* **1987**, *48*, 593–601. [[CrossRef](#)]
38. Massey, H.S.W.; Moiseiwitsch, B.L. The application of variational methods to atomic scattering problems—I. The elastic scattering of electrons by hydrogen atoms. *Proc. R. Soc. Lond. Ser. A Math. Phys. Sci.* **1951**, *205*, 483–496. [[CrossRef](#)]
39. Bates, D.R.; Griffing, G. Inelastic Collisions between Heavy Particles I: Excitation and Ionization of Hydrogen Atoms in Fast Encounters with Protons and with other Hydrogen Atoms. *Proc. Phys. Soc. Sect. A* **1953**, *66*, 961–971. [[CrossRef](#)]
40. Mott, N.F.; Massey, H.S.W. *Theory of Atomic Collisions*, 3rd ed.; Monographs on Physics; Oxford University Press: London, UK, 1965.
41. Feng, Y.P.; Spector, H. Scattering of screened excitons by free carriers in semiconducting quantum well structures. *IEEE J. Quantum Electron.* **1988**, *24*, 1659–1663. [[CrossRef](#)]
42. Rytova, S.N. The Screened Potential of a Point Charge in a Thin Film. *arXiv* **2018**, arXiv:1806.00976.
43. Keldysh, L.V. Coulomb interaction in thin semiconductor and semimetal films. *Sov. J. Exp. Theor. Phys. Lett.* **1979**, *29*, 658.
44. Li, P.; Appelbaum, I. Excitons without effective mass: Biased bilayer graphene. *Phys. Rev. B* **2019**, *99*, 035429. [[CrossRef](#)]
45. Versteegh, M.A.M.; Kuis, T.; Stoof, H.T.C.; Dijkhuis, J.I. Ultrafast screening and carrier dynamics in ZnO: Theory and experiment. *Phys. Rev. B* **2011**, *84*, 035207. [[CrossRef](#)]
46. Quintela, M.F.C.M.; Henriques, J.C.G.; Tenório, L.G.M.; Peres, N.M.R. Theoretical Methods for Excitonic Physics in 2D Materials. *Phys. Status Solidi (B)* **2022**, *259*, 2200097. [[CrossRef](#)]
47. Gomes, J.N.S.; Trallero-Giner, C.; Vasilevskiy, M.I. Variational calculation of the lowest exciton states in phosphorene and transition metal dichalcogenides. *J. Phys. Condens. Matter* **2021**, *34*, 045702. [[CrossRef](#)]
48. Lee, Y.C.; Lin, D.L. Wannier excitons in a thin crystal film. *Phys. Rev. B* **1979**, *19*, 1982–1989. [[CrossRef](#)]
49. Yang, X.L.; Guo, S.H.; Chan, F.T.; Wong, K.W.; Ching, W.Y. Analytic solution of a two-dimensional hydrogen atom. I. Nonrelativistic theory. *Phys. Rev. A* **1991**, *43*, 1186–1196. [[CrossRef](#)]
50. Wannier, G.H. The Structure of Electronic Excitation Levels in Insulating Crystals. *Phys. Rev.* **1937**, *52*, 191–197. [[CrossRef](#)]
51. Serway, R.A.; Faughn, J.S.; Moses, C.J. *College Physics*; Number Volume 1 in College Physics; Brooks/Cole: Devon, UK, 2003.
52. Ferreira, F.; Chaves, A.J.; Peres, N.M.R.; Ribeiro, R.M. Excitons in hexagonal boron nitride single-layer: A new platform for polaritonics in the ultraviolet. *J. Opt. Soc. Am. B* **2019**, *36*, 674–683. [[CrossRef](#)]
53. Henriques, J.C.G.; Ventura, G.B.; Fernandes, C.D.M.; Peres, N.M.R. Optical absorption of single-layer hexagonal boron nitride in the ultraviolet. *J. Phys. Cond. Matter* **2020**, *32*, 025304. [[CrossRef](#)]
54. Selig, M.; Berghäuser, G.; Raja, A.; Nagler, P.; Schüller, C.; Heinz, T.F.; Korn, T.; Chernikov, A.; Malic, E.; Knorr, A. Excitonic linewidth and coherence lifetime in monolayer transition metal dichalcogenides. *Nat. Commun.* **2016**, *7*, 13279. [[CrossRef](#)]
55. Zhang, Z.; Guo, W. Controlling the Functionalizations of Hexagonal Boron Nitride Structures by Carrier Doping. *J. Phys. Chem. Lett.* **2011**, *2*, 2168–2173. [[CrossRef](#)]
56. Majety, S.; Doan, T.C.; Li, J.; Lin, J.Y.; Jiang, H.X. Electrical transport properties of Si-doped hexagonal boron nitride epilayers. *AIP Adv.* **2013**, *3*, 122116. [[CrossRef](#)]
57. He, B.; Qiu, M.; Yuen, M.F.; Zhang, W.J. Electrical properties and electronic structure of Si-implanted hexagonal boron nitride films. *Appl. Phys. Lett.* **2014**, *105*, 012104. [[CrossRef](#)]
58. Sun, F.; Hao, Z.; Liu, G.; Wu, C.; Lu, S.; Huang, S.; Liu, C.; Hong, Q.; Chen, X.; Cai, D.; et al. p-Type conductivity of hexagonal boron nitride as a dielectrically tunable monolayer: Modulation doping with magnesium. *Nanoscale* **2018**, *10*, 4361–4369. [[CrossRef](#)]
59. Feng, Y.P.; Spector, H.N. Exciton linewidth due to scattering from free carriers in semiconducting quantum well structures. *Superlattices Microstruct.* **1987**, *3*, 459–461. [[CrossRef](#)]
60. Feng, Y.P. Excitons in Semiconducting Quantum Well Structures. Ph.D. Thesis, Illinois Institute of Technology, Chicago, IL, USA, 1989.
61. Koh, T.S.; Feng, Y.P.; Spector, H.N. Exciton linewidth due to scattering by free carriers in semiconducting quantum well structures: Finite confining potential model. *J. Appl. Phys.* **1997**, *81*, 2236–2240. [[CrossRef](#)]

62. Kythe, P.K.; Puri, P. *Computational Methods for Linear Integral Equations*; Birkhäuser: Boston, MA, USA, 2002.
63. Du, Y.; Neal, A.T.; Zhou, H.; Ye, P.D. Transport studies in 2D transition metal dichalcogenides and black phosphorus. *J. Phys. Condens. Matter* **2016**, *28*, 263002. [[CrossRef](#)]
64. Kuiri, M.; Srivastav, S.K.; Ray, S.; Watanabe, K.; Taniguchi, T.; Das, T.; Das, A. Enhanced electron-phonon coupling in doubly aligned hexagonal boron nitride bilayer graphene heterostructure. *Phys. Rev. B* **2021**, *103*, 115419. [[CrossRef](#)]
65. Li, J.; Goryca, M.; Yumigeta, K.; Li, H.; Tongay, S.; Crooker, S.A. Valley relaxation of resident electrons and holes in a monolayer semiconductor: Dependence on carrier density and the role of substrate-induced disorder. *Phys. Rev. Mater.* **2021**, *5*, 044001. [[CrossRef](#)]
66. Lampert, M.A. Mobile and Immobile Effective-Mass-Particle Complexes in Nonmetallic Solids. *Phys. Rev. Lett.* **1958**, *1*, 450–453. [[CrossRef](#)]
67. Kheng, K.; Cox, R.T.; d'Aubigné, M.Y.; Bassani, F.; Saminadayar, K.; Tatarenko, S. Observation of negatively charged excitons X^- in semiconductor quantum wells. *Phys. Rev. Lett.* **1993**, *71*, 1752–1755. [[CrossRef](#)]
68. Chen, G.; Stievater, T.H.; Batteh, E.T.; Li, X.; Steel, D.G.; Gammon, D.; Katzer, D.S.; Park, D.; Sham, L.J. Biexciton Quantum Coherence in a Single Quantum Dot. *Phys. Rev. Lett.* **2002**, *88*, 117901. [[CrossRef](#)]
69. Li, X.; Wu, Y.; Steel, D.; Gammon, D.; Stievater, T.H.; Katzer, D.S.; Park, D.; Piermarocchi, C.; Sham, L.J. An All-Optical Quantum Gate in a Semiconductor Quantum Dot. *Science* **2003**, *301*, 809–811. [[CrossRef](#)]